Characterization of Hydrogen-Bond Breaking and Surface Reconstruction in Mixed-Valence Chain Compounds $[Pt(en)_2][Pt(en)_2X_2](ClO_4)_4$ by Atomic Force Microscopy

G. Bar, B. Scott, S. R. Johnson, and B. I. Swanson*

Chemical Science and Technology Group (CST-14), Los Alamos National Laboratory, Los Alamos, New Mexico 87545

J. Ren and M.-H. Whangbo*

Department of Chemistry, North Carolina State University, Raleigh, North Carolina 27695-8204

Received September 19, 1994. Revised Manuscript Received December 12, 1994[⊗]

Mixed-valence compounds $[Pt(en)_2][Pt(en)_2I_2](ClO_4)_4$ and $[Pt(en)_2][Pt(en)_2(Br_{0.8}I_{0.2})_2](ClO_4)_4$ (en = 1,2-diaminoethane) were examined by atomic force microscopy (AFM), and the obtained images were analyzed by calculating the total electron density plots of their surfaces. The patterns of the AFM images are dominated by the most protruded H atoms of the en ligands and the most protruded O atoms of the ClO_4^- anions. The AFM image of $[Pt(en)_2][Pt(en)_2I_2](ClO_4)_4$ shows patterns of the *bc* plane surface expected from the bulk crystal structure. The AFM image of $[Pt(en)_2][Pt(en)_2(Br_{0.8}I_{0.2})_2](ClO_4)_4$ is generally consistent with the *ab* plane surface expected from the bulk structure, but the pattern representing the ClO_4^- anions differs substantially from that expected from the bulk crystal structure. This discrepancy is explained in terms of a rearrangement involving the lower-lying ClO_4^- anions at the *ab* plane surface. Analysis of the N–H···O and C–H···O hydrogen bond contacts suggests that these ClO_4^- anions optimize their N–H···O hydrogen bonding interactions with the help of this rearrangement.

Introduction

Among mixed-valence chain compounds,[1] the halogen-bridged platinum complexes $[Pt(en)_2][Pt(en)_2X_2](ClO_4)_4$ (en = 1,2-diaminoethane; X = Cl, Br, I) are most widely studied. These highly anisotropic compounds are susceptible to a Peierls distortion,[2] so the bridging halogen atoms are displaced from the middle positions between adjacent metal atoms (Figure 1a) thereby leading to an X···Pt–X bond alternation. The associated charge disproportionation is often described as a charge density wave (CDW). Experimentally, the CDW strength can be measured as the ratio of the short to long PtX bond lengths (Pt–X/Pt···X), the smaller ratio representing a stronger CDW. The electron–electron and electron–phonon interactions of these materials, and hence the CDW strengths, can be tuned over a wide range by applying pressure and by changing the bridging halogen atoms, the amine ligands, the metal atoms, and the counterions.[3] Recently, single crystals of mixed halogen chain compounds $[Pt(en)_2][Pt(en)_2(X_{1-y}X'_y)_2](ClO_4)_4$ (X, X′ = halogen; y = 0.0–1.0) have been grown and investigated.[4] The chains of these compounds contain different chain segments of various lengths, and the junctions between the segments give rise to unusual phenomena such as photoinduced charge separation and charge injection.

The electronic and optical properties of mixed-valence chain compounds have been studied by resonance Raman,[5] EPR,[6] and IR[7] spectroscopy. They have also been studied theoretically[8,9] including electronic band structure calculations,[8a] lattice dynamics, and many-body calculations.[9] The predicted and observed photoinduced charge separation and charge injection in mixed-halide crystals makes them potential candidates for photovoltaic and photoconductive devices. Synthetic control of the segment distribution in these systems can open the

[⊗] Abstract published in *Advance ACS Abstracts,* January 15, 1995.

(1) (a) Miller, J. S.; Epstein, A. J. *Prog. Inorg. Chem.* **1976**, *20*, 1. (b) Keller, H. J. In *Extended Linear Chain Compounds*; Miller, J. S., Ed.; Plenum: New York, 1982; Vol. 3. (c) Clark, R. J. H.; Croud, V. B. In *Organic and Inorganic Lowdimensional Crystalline Materials*; Delhaes, P., Drillon, M., Eds.; Plenum: New York, 1987.

(2) Peierls, R. E. *Quantum Theory of Solids*; Oxford University Press: London, 1955; p 108.

(3) (a) Scott, B.; Donohoe, R. J.; Johnson, S. R.; Wilkerson, M. P.; Swanson, B. I. *Synth. Met.* **1993**, *56*, 3426. (b) Okamoto, H.; Mitani, T.; Toriumi, K.; Yamashita, M. *Mater. Sci. Eng.* **1992**, *B13*, L9. (c) Kuroda, N.; Sakai, M.; Nishina, Y.; Sasaki, K. *Phys. Rev. Lett.* **1992**, *68*, 3056.

(4) (a) Worl, L. A.; Huckett, S. C.; Swanson, B. I.; Saxena, A.; Bishop, A. R.; Gammel, J. T. *J. Phys.: Condensed Matter* **1992**, *4*, 10239. (b) Scott, B.; Johnson, S. R.; Swanson, B. I. *Synth. Met.* **1993**, *56*, 3432.

(5) (a) Clark, R. J. H. In *Advances in Infrared and Raman Spectroscopy*; Clark, R. J. H., Hester, R. E., Eds.; Wiley Heyden: New York, 1984; Vol. 11. (b) Tanaka, M.; Kurita, S. J. *J. Phys. C* **1986**, *19*, 3019. (c) Donohoe, R. J.; Worl, L. A.; Arrington, C. A.; Bulou, A.; Swanson, B. I. *Phys. Rev B* **1992**, *45*, 185.

(6) (a) Haruki, M.; Kurita, S. *Phys. Rev. B* **1989**, *39*, 5706. (b) Kuroda, N.; Sakai, M.; Suezawa, M.; Nishina, Y.; Sumino, K. *J. Phys. Soc. Jpn.* **1990**, *59*, 3049.

(7) (a) DeGiorgi, L.; Wachter, P.; Haruki, M.; Kurita, S. *Phys. Rev. B* **1989**, *40*, 3285. (b) Love, S. P.; Huckett, S. C.; Worl, L. A.; Frankcom, T. M.; Ekberg, S. A.; Swanson, B. I. *Phys. Rev. B* **1993**, *47*, 11107.

(8) (a) Whangbo, M.-H.; Foshee, M. J. *Inorg. Chem.* **1981**, *20*, 113. (b) Onodera, Y. *J. Phys. Soc. Jpn.* **1987**, *56*, 250. (c) Mishima, A.; Nasu, K. *Phys. Rev. B* **1989**, *39*, 5758.

(9) (a) Bulou, A.; Donohoe, R. J.; Swanson, B. I. *J. Phys.: Condensed Matter* **1991**, *3*, 1709. (b) Gammel, J. T.; Donohoe, R. J.; Bishop, A. R.; Swanson, B. I. *Phys. Rev. B* **1990**, *42*, 10566.

0897-4756/95/2807-0391$09.00/0

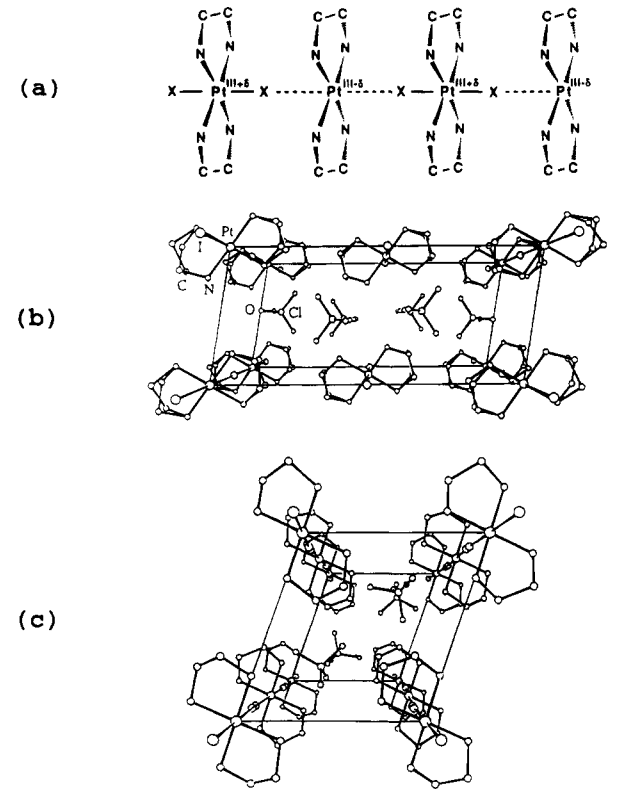

Figure 1. (a) Schematic view of a $[Pt(en)_2][Pt(en)_2X_2]$ chain. (b) Perspective view of the crystal structure of $[Pt(en)_2][Pt(en)_2I_2](ClO_4)_4$. The en groups are disordered to have two conformations as shown in this diagram. (c) Perspective view of the crystal structure of $[Pt(en)_2][Pt(en)_2(Br_{0.8}I_{0.2})_2](ClO_4)_4$. The projection in (b) and (c) is along the chain axis (*b* axis). Hydrogen atoms are not shown for the sake of clarity.

door to a new class of materials. For a clear understanding of the segment-distribution, it is essential to examine the long-range structure and the short-range structure including defects. To obtain such information, it is appealing to employ the real-space surface-analysis methods such as scanning tunneling microscopy (STM)[10,11] and atomic force microscopy (AFM).[12,13] So far, the surfaces of the mixed-valence compounds $[Pt(en)_2][Pt(en)_2X_2](ClO_4)_4$ and $[Pt(en)_2][Pt(en)_2(X_{1-y}X'_y)_2](ClO_4)_4$ have not been characterized.

Crystal samples of these compounds are needle- or platelike, and their surfaces have the chains running along the needle direction. Therefore, the surfaces are composed of the ethylene groups of the en ligands as well as ClO_4^- anions. In the bulk crystal structures, the ClO_4^- anions link the adjacent chains via the N−H···O and C−H···O hydrogen bonds. Some of these hydrogen bonds are truncated at the sample surfaces. This will make the forces acting on the surface ClO_4^- anions unbalanced, which may lead to a surface reconstruction. In principle, it should be possible to detect the latter by STM and AFM, since both can provide atomic or molecular resolution images of surfaces. STM is applicable only to metals and semiconductors, as it requires measurable tunneling currents between the sample and scanning tip. However, AFM is applicable to all materials including insulators because the probing interactions between the sample and tip are universal (i.e., repulsive forces in a contact-mode AFM). Our attempt to characterize $[Pt(en)_2][Pt(en)_2I_2](ClO_4)_4$ and $[Pt(en)_2][Pt(en)_2(Br_{0.8}I_{0.2})_2](ClO_4)_4$ by STM was unsuccessful because they are not conductive enough. In the present work, we report results of our AFM measurements on these two compounds and discuss how the breaking of the N−H···O and C−H···O hydrogen bonds at the surface affects the arrangements of the surface ClO_4^- anions.

Experimental Section

The compounds $[Pt(en)_2][Pt(en)_2I_2](ClO_4)_4$ and $[Pt(en)_2][Pt(en)_2(Br_{0.8}I_{0.2})_2](ClO_4)_4$ were prepared by the methods described previously.[4b,14] We also prepared and studied $[Pt(en)_2][Pt(en)_2Br_2](ClO_4)_4$, as will be mentioned below. The platelike $[Pt(en)_2][Pt(en)_2I_2](ClO_4)_4$ and needlelike $[Pt(en)_2][Pt(en)_2(Br_{0.8}I_{0.2})_2](ClO_4)_4$ samples were mounted on a support with no special surface treatment before imaging. Our AFM experiments were performed at ambient conditions with a commercial scanning probe microscope, Nanoscope III. Cantilevers with pyramidal shaped Si_3N_4 tips (force constants of 0.12 N/m) were used for AFM measurements. We checked the *z* calibration of the instrument by measuring monoatomic steps of Au(111) substrates. Large-scale images were registered in the height-imaging mode and molecular scale images in the height and force imaging mode.[15]

Not all crystal faces are suitable for AFM imaging, e.g., the side face of $[Pt(en)_2][Pt(en)_2I_2](ClO_4)_4$ is too narrow and rough to obtain molecular-resolution images. Our measurements were performed on the largest crystal faces. To determine and confirm the crystal surfaces imaged by AFM, a Laue photograph was used for $[Pt(en)_2][Pt(en)_2I_2](ClO_4)_4$, and a fully automated Siemans R3m/pc diffractometer for $[Pt(en)_2][Pt(en)_2(Br_{0.8}I_{0.2})_2](ClO_4)_4$.

Our measurements with several different crystal samples and with different tips led to reproducible images. Samples of $[Pt(en)_2][Pt(en)_2I_2](ClO_4)_4$ are preferentially cleaved along the *bc* plane. Identical results were obtained from our measurements of as-grown and cleaved surfaces, so the characteristic features of the AFM images (see below) are not associated with foreign species adsorbed on the surface. Samples of $[Pt(en)_2][Pt(en)_2(Br_{0.8}I_{0.2})_2](ClO_4)_4$ are not easily cleaved, so that only as-grown surfaces were examined.

To improve the quality of the images and accurately assign the observed patterns, the images were taken at several different scanning directions of the tip with respect to the surface. Thermal drift induces nonorthogonality into the tip scanning pattern thereby leading to an artificial distortion of the unit cell size and symmetry. To minimize this effect, we made sure that the instrument is stabilized thermally before measurements. The effect of thermal drift cannot be removed completely, and its presence is readily spotted because it varies in a systematic way with scan direction and rate. Hundreds of images in the "up" and "down" scan directions were captured, and the averaged data were used for image characterization.

(10) Binnig, G.; Rohrer, H.; Gerber, Ch.; Weibel, E. *Phys. Rev. Lett.* **1981**, *49*, 57.

(11) For recent reviews, see: (a) *Scanning Tunneling Microscopy I and II*; Wiesendanger, R., Güntherodt, H.-J., Eds.; Springer-Verlag: Heidelberg, 1992. (b) *Scanning Tunneling Microscopy*; Stroscio, J. A., Kaiser, W. J., Eds.; Academic Press: San Diego, 1993; Vol. 27.

(12) Binnig, G.; Quate, C. F.; Gerber, Ch. *Phys. Rev. Lett.* **1986**, *56*, 930.

(13) For recent reviews, see: (a) Meier, E.; Heinzelmann, H. In *Scanning Tunneling Microscopy II*; Wiesendanger, R., Güntherodt, H.-J., Eds.; Springer-Verlag: Heidelberg, 1992; p 99. (b) Sarid, D. *Scanning Force Microscopy*; Lapp, M., Stark, H., Eds.; Oxford University Press: New York, 1991.

(14) Huckett, S. C.; Donohoe, R. J.; Worl, L. A.; Bulou, A.; Burns, C. J.; Laia, J. R.; Carroll, D.; Swanson, B. I. *Chem. Mater.* **1991**, *3*, 123.

(15) In the height imaging mode, the feedback gains are set high so that the tip follows the contour of constant interatomic forces. In the force imaging mode, the feedback gains are set low so that the tip moves at a constant height while registering the variation of interatomic force.

Some images were filtered by using the fast Fourier transform (FFT) procedure to enhance the periodic features. In this procedure only the most pronounced frequency patterns of the FFT power spectrum are chosen to reconstruct an idealized image by the inverse FFT.

Crystal Structures

The crystal structure of $[Pt(en)_2][Pt(en)_2I_2](ClO_4)_4$ is illustrated in Figure 1b. The compound crystallizes in the monoclinic space group C2/m with cell parameters a = 16.901 Å, b = 5.805 Å, c = 7.448 Å, and β = 98.74°.[16,17] The chains run along the b axis, and the ClO_4^- anions link the chains by making N−H···O and C−H···O hydrogen bonds with their en ligands. Since the Pt atom sits on a site of $C2/m$ symmetry, the C atom positions of the en ligand are disordered. Thus, each en ligand assumes one of the two possible nonplanar conformations. All ClO_4^- anions are crystallographically equivalent.

$[Pt(en)_2][Pt(en)_2Br_2](ClO_4)_4$ crystallizes in the monoclinic space group $P2_1/m$ with cell parameters a = 7.972(3) Å, b = 10.874(3) Å, c = 8.500(4) Å, and β = 108.91(4)°.[18] $[Pt(en)_2][Pt(en)_2Br_2](ClO_4)_4$ has a monoclinic-to-orthorhombic phase transition around room temperature (29 °C),[18] while $[Pt(en)_2][Pt(en)_2I_2](ClO_4)_4$ exhibits no such phase change. The transition temperature is raised when $[Pt(en)_2][Pt(en)_2Br_2](ClO_4)_4$ is doped with $[Pt(en)_2][Pt(en)_2I_2](ClO_4)_4$. In $[Pt(en)_2][Pt(en)_2Br_2](ClO_4)_4$, the C atom positions of each en ligand are ordered, because each five-membered ring made up of a Pt atom and an en ligand assumes only one of the two possible nonplanar conformations. There are two crystallographically nonequivalent ClO_4^- anions.

$[Pt(en)_2][Pt(en)_2(Br_{0.8}I_{0.2})_2](ClO_4)_4$ has a monoclinic cell at room temperature and adopts the structure of pure $[Pt(en)_2][Pt(en)_2Br_2](ClO_4)_4$ (Figure 1c).[17] It undergoes a monoclinic-to-orthorhombic phase transition around room temperature.[18] The unit-cell parameters of this mixed halogen compound are a = 7.963(2) Å, b = 11.020(2) Å, c = 8.553(2) Å, and β = 109.52(2)°.[18] As in pure $[Pt(en)_2][Pt(en)_2I_2](ClO_4)_4$, the chains are aligned along the b axis, and the ClO_4^- anions lie between the chains. The $[Pt(en)_2][Pt(en)_2Br_2](ClO_4)_4$ segments of $[Pt(en)_2][Pt(en)_2(Br_{0.8}I_{0.2})_2](ClO_4)_4$ are basically the same in structure as pure $[Pt(en)_2][Pt(en)_2Br_2](ClO_4)_4$. However, the $[Pt(en)_2][Pt(en)_2I_2](ClO_4)_4$ segments are slightly different in structure from pure $[Pt(en)_2][Pt(en)_2I_2](ClO_4)_4$. The $[Pt(en)_2][Pt(en)_2I_2]$ segments, residing in the smaller $[Pt(en)_2][Pt(en)_2Br_2]$ lattice, are compressed along the chain direction. The latter decreases the long Pt···I bond and hence the strength of the CDW.

It is of interest to note that for both $[Pt(en)_2][Pt(en)_2Br_2](ClO_4)_4$ and $[Pt(en)_2][Pt(en)_2(Br_{0.8}I_{0.2})_2](ClO_4)_4$,[18] the isotropic thermal parameters of the O atoms (of the ClO_4^- ions) are much higher for the orthorhombic (higher temperature) phase than for the monoclinic (lower temperature) phase. The O atoms make hydrogen bonds with the N−H and C−H bonds of the en groups (see below). Thus, the increased thermal motions of the O atoms in the orthorhombic phase imply a weakening of the hydrogen-bond network. The monoclinic-to-orthorhombic phase transition in the two compounds may be reviewed as caused by a weakening of the hydrogen-bond network, because the thermal motions of the ClO_4^- ions increase with increasing temperature, thereby weakening the hydrogen-bond network.

Image Simulation by Electron Density Plot Calculations

High-resolution STM and AFM images were obtained for a large number of molecular crystals[19] and layered materials.[20] To a first approximation, the STM image of a surface is described by the partial density plot of the surface, $\varrho(r_0,e_f)$,[21] the density associated with the energy levels near the Fermi level e_f. The AFM image of a surface obtained with a contact mode is described by the total density plot of the surface, $\varrho(r_0)$. Recently, the STM and AFM images of various layered transition-metal compounds and organic conducting salts were successfully interpreted[22] on the basis of the $\varrho(r_0,e_f)$ and $\varrho(r_0)$ plots calculated by the extended Hückel tight-binding (EHTB) electronic band structure method.[23] Other methods used for image simulations include first principles calculations for STM[21a,24] and molecular mechanics calculations for AFM.[25] In the present study, the AFM images of $[Pt(en)_2][Pt(en)_2I_2](ClO_4)_4$ and $[Pt(en)_2][Pt(en)_2(Br_{0.8}I_{0.2})_2](ClO_4)_4$ are simulated by calculating their $\varrho(r_0)$ plots on the basis of the EHTB electronic band structure method.

AFM Images of $[Pt(en)_2][Pt(en)_2I_2](ClO_4)_4$

Figure 2a shows a large-scale AFM image of $[Pt(en)_2][Pt(en)_2I_2](ClO_4)_4$. Atomically flat terraces with several steps are clearly visible. The step heights are mostly about 8 Å, which is half the thickness of the unit cell along the a axis (16.9 Å). The terraces and steps extend along the b direction (i.e., the chain direction), and they correspond to the bc cleavage plane. Areas corresponding to molecular flatness as large as 60 × 60 nm^2 can be observed. Figure 2b shows a typical small-scale AFM height image of $[Pt(en)_2][Pt(en)_2I_2](ClO_4)_4$. Similar images are obtained with the force imaging mode. The AFM image consists of two different rows of patterns aligned along the b direction. The surface unit cell

(16) Endres, H.; Keller, H. J.; Martin, R.; Gung, H. N.; Traeger, U. *Acta Crystallogr.* **1979**, *B35*, 1885.
(17) Scott, B., unpublished.
(18) Huckett, S. C.; Scott, B.; Love, S. P.; Donohoe, R. J.; Burns, C. J.; Garcia, E.; Frankcom, T.; Swanson, B. I. *Inorg. Chem.* **1993**, *32*, 2137.
(19) (a) Yoshimura, M.; Shigekawa, H.; Nejoh, H.; Saito, G.; Saito, Y.; Kawazu, A. *Phys. Rev. B* **1991**, *43*, 13590. (b) Bar, G.; Magonov, S. N.; Cantow, H.-J.; Kushch, N.; Yagubskii, E. B.; M-H.; Liang, W.; Ren, J.; Whangbo, M.-H. *New J. Chem.* **1993**, *17*, 439. (c) Fainchtein, R.; D'Archangelis, S. T.; Yang, S. S.; Cowan, D. O. *Science* **1992**, *256*, 1012. (d) Li, S.; White, H. S.; Ward, M. D. *J. Phys. Chem.* **1992**, *96*, 9014. (e) Campos, C. E.; Dubois, J. G. A.; Gerritsen, J. W.; Tibbitts, T. T.; Brooks, J. S.; van Kempen, H.; Tokumoto, M.; Kinoshita, N.; Tanaka, Y. *Phys. Rev. Lett.* **1993**, *71*, 1720.
(20) (a) Stupian, G. W.; Leung, M. S. *Appl. Phys. Lett.* **1987**, *51*, 1560. (b) Akari, S.; Stachel, M.; Birk, H.; Schreck, E.; Lux, M.; Dransfeld, K. *J. Microsc.* **1988**, *152*, 521. (c) Lieber, C. M.; Xu, X. L. *Acc. Chem. Res.* **1991**, *24*, 170. (d) Dai, Z.; Xue, Q.; Slough, C. G.; Coleman, R. V. *Phys. Rev. B* **1993**, *48*, 14543.
(21) (a) Tersoff, J.; Hamman, D. R. *Phys. Rev. B* **1985**, *31*, 805. (b) Tersoff, J. *Phys. Rev. Lett.* **1986**, *57*, 440.
(22) Magonov, S. N.; Whangbo, M.-H. *Adv. Mater.* **1994**, *6*, 355.
(23) Whangbo, M.-H.; Hoffmann, R. *J. Am. Chem. Soc.* **1978**, *100*, 6093.
(24) (a) Watanabe, S.; Aono, M.; Tsukada, M. *Ultramicroscopy* **1992**, *42–44*, 105. (b) Watanabe, S.; Aono, M.; Tsukada, M. *J. Vac. Sci. Technol. B* **1994**, *12*, 2167.
(25) Tang, H.; Joachim, C.; Devillers, J. *J. Vac. Sci. Technol. B* **1994**, *12*, 2179.

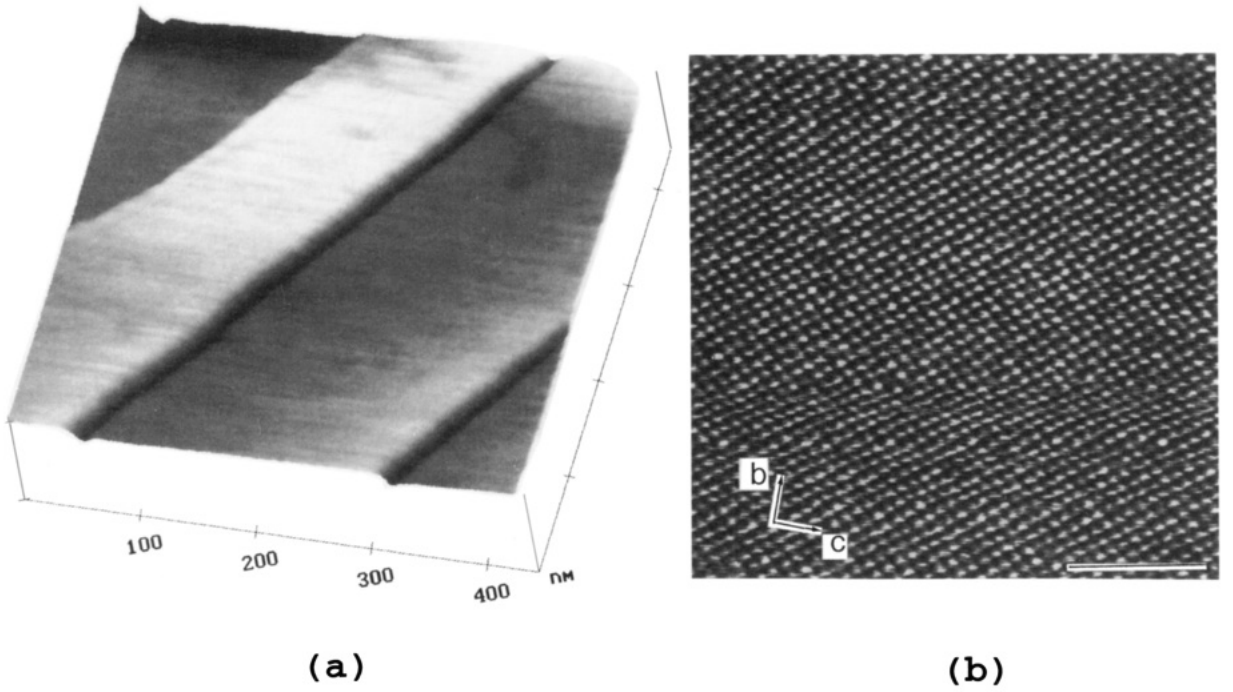

Figure 2. (a) Large-scale AFM height image of the *bc* plane surface of $[Pt(en)_2][Pt(en)_2I_2](ClO_4)_4$ showing steps with heights of half the *a* parameter. (b) Small scale AFM image of the *bc* plane surface of $[Pt(en)_2][Pt(en)_2I_2](ClO_4)_4$ obtained in the height imaging mode. The horizontal bar corresponds to 5 nm. The gray contrast shows height variations in nanometers in the range 0.0−0.8 nm with brighter spots representing more elevated places. No image processing besides a plane subtraction was applied.

parameters of the images ($b = 5.7 \pm 0.2$ Å, $c = 7.4 \pm 0.3$ Å, and $\alpha = 90° \pm 3°$) are consistent with the *bc* plane parameters of the bulk crystal. A Laue photograph taken for the same sample surface results in the lattice parameters consistent with the *bc* plane surface. Thus, the observed AFM image corresponds to the *bc* plane surface.

Figure 3a shows a filtered image for a zoomed part of Figure 2b. The structure of the *bc* plane surface expected from the bulk crystal structure is depicted in Figure 3b, where only one of the two possible en conformations is shown. The most protruded atoms of the surface are the ethylene H atoms of the en ligands, which are about 0.6 Å higher than the protruded O atoms of the ClO_4^- anions. The $\varrho(r_0)$ plot of the *bc* plane surface calculated on the basis of the bulk crystal structure is shown in Figure 3c, where the density peaks are located on the most protruded H atoms of en and on the most protruded O atoms of the ClO_4^- anions. The ethylene H atoms contribute more to the $\varrho(r_0)$ plot than do the O atoms of the ClO_4^- ions, since the protruded H atoms lie higher than the protruded O atoms by about 0.6 Å. The bigger and brighter spots of the AFM image are assigned to the ethylene group H atoms, and the smaller spots to the anion O atoms. Since an O atom is surrounded by more electrons than is a H atom, the effective height difference between the most protruded O and H atoms of the *bc* plane surface is smaller than 0.6 Å. Thus, the AFM image reveals the features of the *bc* plane surface expected from the bulk crystal structure. The $\varrho(r_0)$ plot calculated for the alternative en conformation is given in Figure 3d, which exhibits features essentially identical with those of Figure 3c. Therefore, it is not possible to discern from the observed images whether or not the conformations of the surface en ligands are ordered.

AFM Images of $[Pt(en)_2][Pt(en)_2(Br_{0.8}I_{0.2})_2](ClO_4)_4$

A typical AFM height image of $[Pt(en)_2][Pt(en)_2(Br_{0.8}I_{0.2})_2](ClO_4)_4$ is given in Figure 4a, which shows two different rows of patterns aligned along the *b* direction (i.e., the chain direction). We observed similar images of the pure $[Pt(en)_2][Pt(en)_2Br_2](ClO_4)_4$ compound, but molecular-resolution images were obtained more easily and more frequently for the mixed crystals because of the higher crystal quality and stability. Similar images are obtained in the force imaging mode. A filtered image of a zoomed part of Figure 4a is shown in Figure 4b, which reveals two distinguishable rows (brighter and dimmer ones) of slightly different heights. Figure 4c,d respectively shows the profiles of the height corrugations along the d−d and e−e lines of Figure 4b. The bright spots within each row (either the brighter or the dimmer one) have the same heights and form a straight line. The height of the dimmer row is about 0.24 Å lower than that of the brighter row. The surface unit cell parameters of the images (7.9 ± 0.5 Å, 10.8 ± 0.6 Å, $89° \pm 6°$) are consistent either with the *ab* plane [$a = 7.963(2)$ Å, $b = 11.020(2)$ Å, $\gamma = 90.0°$] or with the *bc* plane surface [$b = 11.020(2)$ Å, $c = 8.553(2)$ Å, $\alpha = 90.0°$] of the bulk crystal.

To identify the surface of the needle-shaped crystal imaged by AFM, we oriented the crystal in an X-ray diffractometer and determined the Miller indices of all the crystal planes. Figure 4e shows a schematic cross-section view of the crystal and the associated surface indices determined by this study, which reveals that the imaged surface corresponds to the *ab* plane. There are two points to mention: First, it is possible to deduce which of the *bc* and *ab* plane surfaces (see Figures 5a and 5b, respectively) is the imaged one by considering the details of the surface structures expected from the

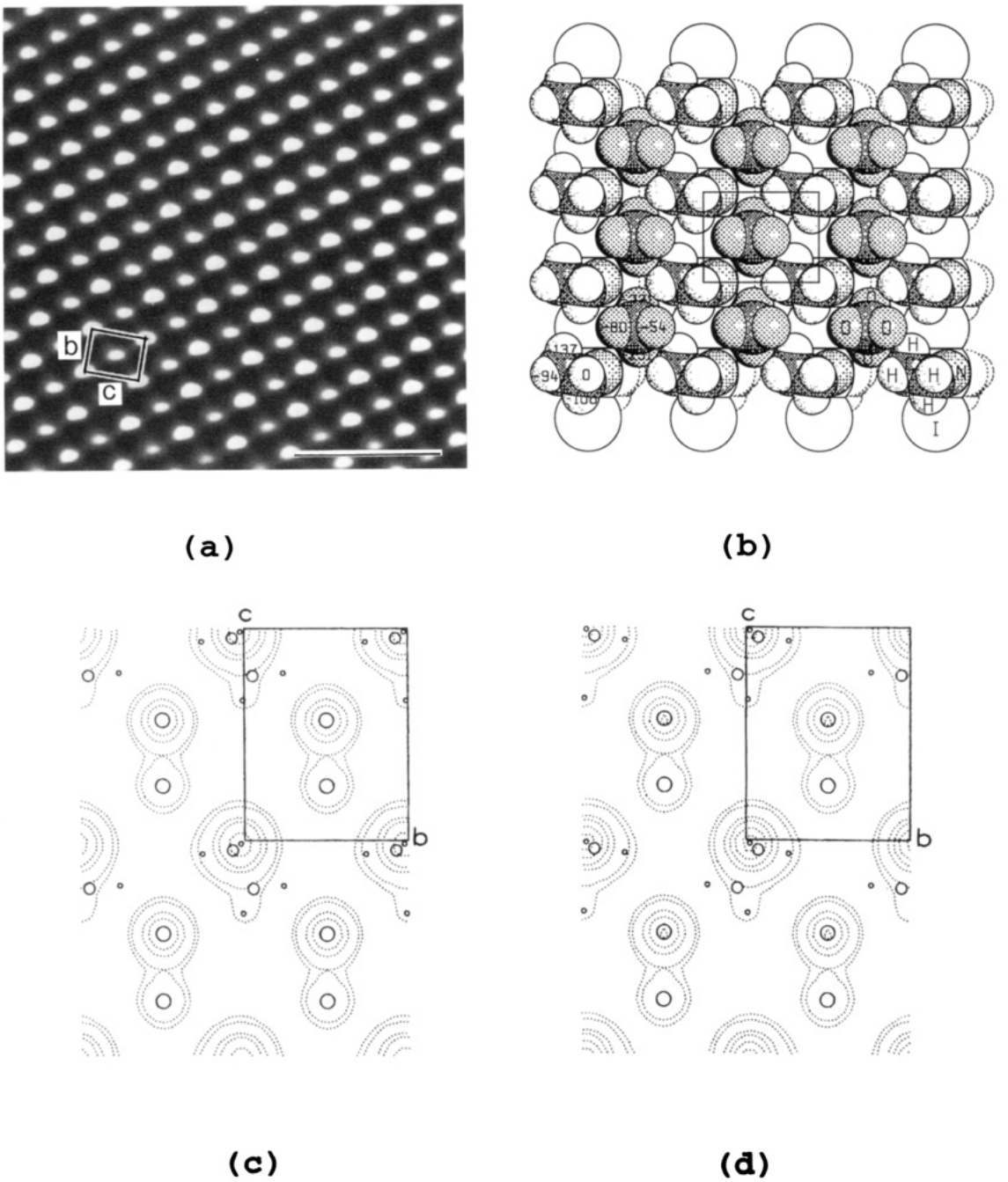

Figure 3. (a) Zoomed part of the AFM image of Figure 2b after FFT filtering and rotation, where the horizontal scale bar corresponds to 2 nm. (b) Space-filling model of the molecular arrangement of the *bc* plane surface of $[Pt(en)_2][Pt(en)_2I_2](ClO_4)_4$ taken from the bulk crystal structure. The numbers within the circles representing surface atoms indicate their relative heights in picometers. The most protruded atom is assigned a value of 0 pm, while the lower lying atoms have negative values. (c) $\varrho(r_0)$ plot of the *bc* plane surface of $[Pt(en)_2][Pt(en)_2I_2](ClO_4)_4$, in which the en ligands adopt one conformation. (d) $\varrho(r_0)$ plot of the *bc* plane surface of $[Pt(en)_2][Pt(en)_2I_2](ClO_4)_4$, in which the en ligands adopt the alternative conformation. In (c) and (d), the contour values used are 400, 200, 100, 50, 10, and 5×10^{-4} electrons/au^3. Only the ethylene groups of the en ligands and the most protruded O atoms of the ClO_4^- anions are shown. The small, medium, and large circles represent the H, C, and O atoms, respectively.

bulk crystal structure. In the *bc* plane surface (Figure 5a), the protruded O atoms of the two ClO_4^- anions have a height difference of slightly larger than 1.0 Å, so that only the higher-lying anion can be detected by AFM.[22] In addition, the protruded O atom of the higher-lying anion is raised above the most protruded H atom of the en ligand by nearly 0.8 Å. Since an O atom is surrounded by more electrons than is an H atom, the effective height difference between the most protruded O and H atoms of the *bc* plane surface should be larger than 0.8 Å. Therefore, the $\varrho(r_0)$ plot (not shown) of the *bc* plane surface is dominated by the most protruded O atom of the higher-lying ClO_4^- anion. Consequently, the *bc* plane surface is inconsistent with the AFM images in Figure 4a,b. Second, Figure 4e shows that the $[Pt(en)_2][Pt(en)_2(Br_{0.8}I_{0.2})_2](ClO_4)_4$ sample does not have a *bc* surface. For the $[Pt(en)_2][Pt(en)_2I_2](ClO_4)_4$ samples, the surfaces other than the *bc* face are too narrow and rough to obtain molecular-resolution AFM images. Consequently, it was not possible to image an identical face for the two salts and examine differences in the resulting images.

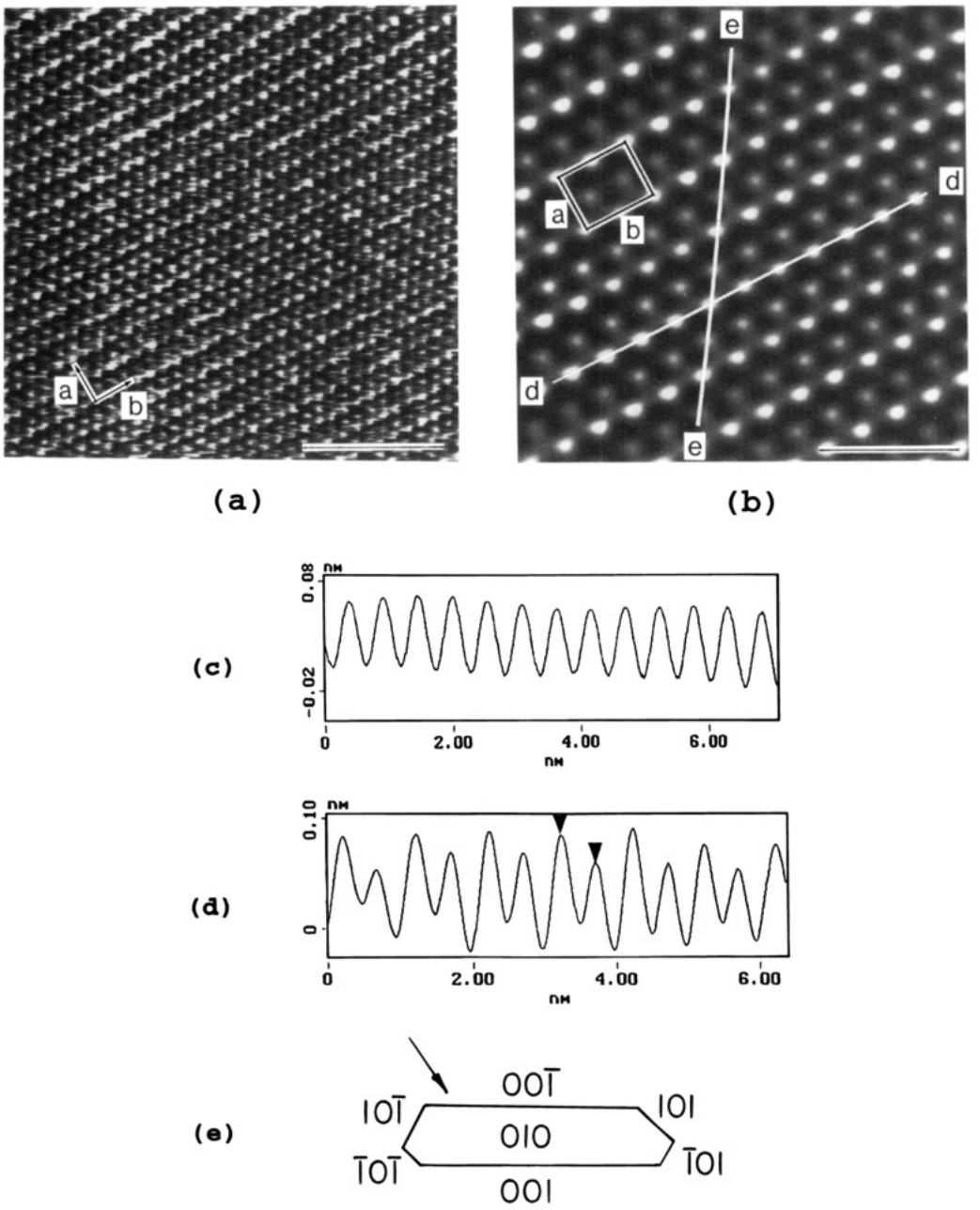

Figure 4. (a) Small-scale AFM image of the *ab* plane surface of $[Pt(en)_2][Pt(en)_2(Br_{0.8}I_{0.2})_2](ClO_4)_4$ obtained with the height imaging mode. The horizontal scale bar corresponds to 5 nm. The gray contrast shows height variations in nanometers in the range 0−0.4 nm and brighter spots correspond to more elevated places. No image processing besides a plane subtraction was applied. (b) Zoomed part of the AFM image of Figure 4a after FFT filtering and rotation, where the horizontal scale bar corresponds to 2 nm. (c) Profile of the *z*-height corrugation along the d−d line of Figure 3b. The height corrugation is negligible. (d) Profile of the *z*-height corrugation along the e−e line of Figure 3b. The height difference between the two marked points is about 0.24 Å in average. (e) Schematic drawing showing a cross section (perpendicular to the *b* axis) of the needlelike $[Pt(en)_2][Pt(en)_2(Br_{0.8}I_{0.2})_2](ClO_4)_4$ crystal sample. The indices of the associated surfaces are also shown. The imaged face is the *ab* plane surface (indicated by an arrow).

In the *ab* plane surface (Figure 5b), the most protruded oxygen atoms of the two ClO_4^- anions have a height difference of slightly less than 0.6 Å, and the most protruded O atoms of the higher-lying ClO_4^- anions lie lower than the most protruded H atoms of the en ligands by only about 0.2 Å. Thus, the $\varrho(r_0)$ plot of the *ab* plane surface (Figure 5c) are almost equally represented by the most protruded O and H atoms of the surface. This prediction is consistent with the observed AFM images of Figure 4a,b. However, in the $\varrho(r_0)$ plot, the protruded O atoms of the two ClO_4^- anions possess significantly different densities and form a zigzag pattern along the *b* axis. This is not in agreement with the experimental AFM image of Figure 4b, regardless of which one of the two different rows is assigned to the anions. It is important to consider a probable cause for this discrepancy. The recent AFM studies of layered transition metal halides and organic conducting salts[22] showed that AFM is quite sensitive to height corrugations in the range 0.3−1.0 Å. In the experimental AFM image of $[Pt(en)_2][Pt(en)_2(Br_{0.8}I_{0.2})_2](ClO_4)_4$, the two ClO_4^- anions appear almost in equal brightness despite the difference in their corrugation height by about 0.6 Å according to the bulk crystal structure, as is the case in Figure 4b regardless of which of the two different rows is considered to represent the

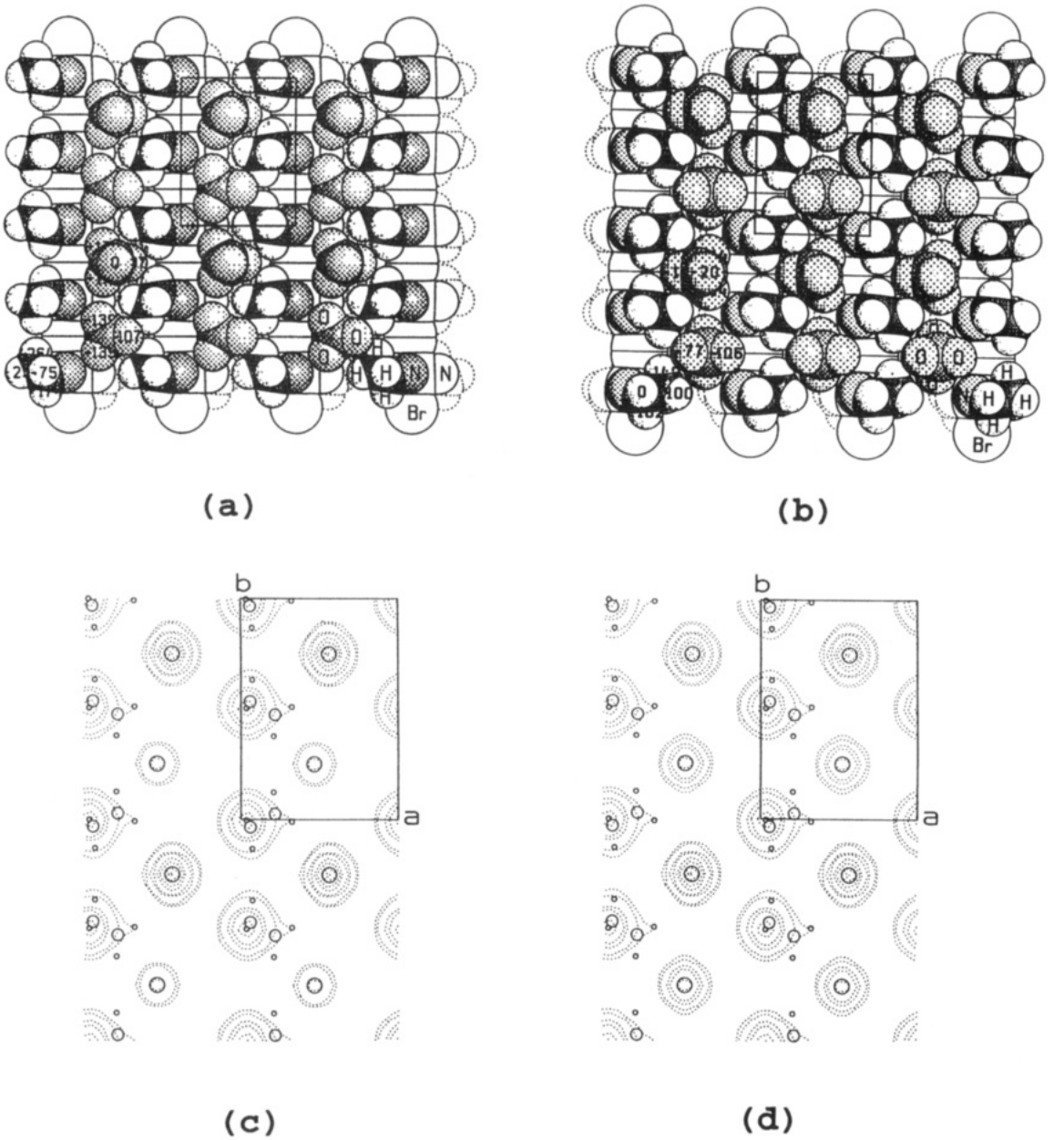

Figure 5. (a) Space-filling model of the molecular arrangement of the *bc* plane surface of $[Pt(en)_2][Pt(en)_2(Br_{0.8}I_{0.2})_2](ClO_4)_4$ taken from the bulk crystal structure. The numbers within the circles have the same meaning as in Figure 3b. (b) Space-filling model of the molecular arrangement of the *ab* plane surface of $[Pt(en)_2][Pt(en)_2(Br_{0.8}I_{0.2})_2](ClO_4)_4$ taken from the bulk crystal structure. The numbers within the circles have the same meaning as in Figure 3b. (c) $\varrho(r_0)$ plot of the *ab* plane surface of $[Pt(en)_2][Pt(en)_2(Br_{0.8}I_{0.2})_2](ClO_4)_4$ calculated on the basis of the bulk crystal structure. (d) $\varrho(r_0)$ plot of the reconstructed *ab* plane surface (see text) of $[Pt(en)_2][Pt(en)_2(Br_{0.8}I_{0.2})_2](ClO_4)_4$. In (c) and (d), the contour values used are 1500, 1000, 500, 300, 100, 50, 10, and 5×10^{-4} electrons/au^3. Only the ethylene groups of the en ligands and the most protruded O atoms of the ClO_4^- anions are shown. The small, medium and large circles represent the H, C, and O atoms, respectively.

anions. This is generally found for various observed images although their resolution depends somewhat on the scanning direction, tip quality, and thermal drift. Consequently, the aforementioned discrepancy between the observed image and the $\varrho(r_0)$ plot suggests strongly the presence of a surface reconstruction in the *ab* plane surface. Indeed, the experimental image can be reproduced if the protruded O atom of the lower-lying ClO_4^- anion (Figure 5b) is raised in height and shifted along the *a*-axis direction so as to form a straight line with the protruded O atom of the higher lying ClO_4^- anion along the *b*-axis direction. This rearrangement can be accomplished in two steps: (1) first, rotate the anion around the axis parallel to the *b* axis and passing through the Cl atom so as to make the Cl−O bond of the protruded O atom almost perpendicular to the surface (see Figure 6c), which reduces the height difference between the protruded O atoms of the two ClO_4^- anion to 0.2 Å; (2) then raise the height of the rotated anion by about 0.2 Å. Figure 5d shows the $\varrho(r_0)$ plot calculated for the *ab* plane surface structure in which the arrangement of the lower-lying ClO_4^- anion is modified by step 1. Clearly, this density plot is close to the experimental AFM image. When the height of the lower-lying anion is further changed by step 2, the agreement between theory and experiment becomes perfect (not shown). We will discuss the energetic reason for why the lower-lying ClO_4^- anions are likely

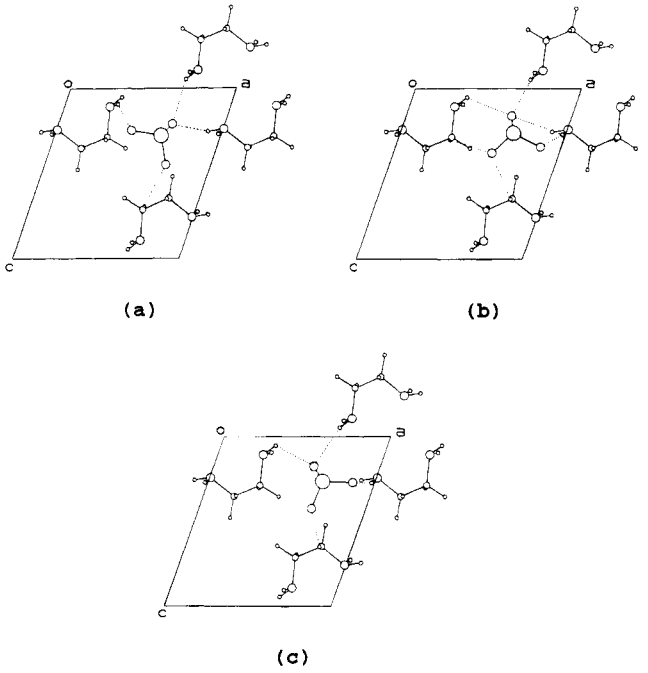

Figure 6. (a) Projection view (along the *b* axis) of the N–H···O and C–H···O hydrogen bonds around the higher-lying ClO_4^- anion expected from the bulk crystal structure. (b) Projection view (along the *b* axis) of the N–H···O and C–H···O hydrogen bonds around the lower-lying ClO_4^- anion expected from the bulk crystal structure. (c) Projection view (along the *b* axis) of the N–H···O and C–H···O hydrogen bonds around the lower-lying ClO_4^- anion when its position is rotated (see text). For simplicity, only the en ligands and ClO_4^- anions are shown in (a)–(c). The smallest and largest circles represent H and Cl, respectively. The short H···O contacts are indicated by dashed lines.

to undergo such a rearrangement in the next section.

Finally, it is noted from Figure 5c,d that the density of the protruded O atom of the higher-lying ClO_4^- anion is larger than that of the protruded H atom of the en ligand, although the O atoms lies lower than the H atom by about 0.2 Å. This reflects the fact that an O atom is surrounded by more electrons than is an H atom. Thus, the rows of the brighter spots in the experimental AFM image (Figure 4a,b) should be assigned to the protruded O atoms of the ClO_4^- anions.

Hydrogen-Bond Breaking and Surface Reconstruction

It has been recognized for some time that hydrogen bonding plays a crucial role in determining the structures of molecular solids and hence their physical properties.[26-29] The crystal structure of $[Pt(en)_2][Pt(en)_2(Br_{0.8}I_{0.2})_2](ClO_4)_4$ shows that each ClO_4^- anion is surrounded with eight en ligands and makes N–H···O and C–H···O hydrogen bonds with them (with H···O contact distances shorter than its van der Waals distance, 2.7 Å). The ClO_4^- anions and the en ligands make almost exclusively N–H···O hydrogen bonds along the *a*- and *b*-axis directions, while they make only C–H···O hydrogen bonds along the *c*-axis direction (see Figure 6). Since a C–H···O hydrogen bond is weaker than an N–H···O hydrogen bond, the chains (running the *b* axis) are more weakly bound along the *c* than along the *a* direction.

Figure 6a shows a projection view (along the *b* axis) of the N–H···O and C–H···O hydrogen bonds around the higher-lying ClO_4^- anion. Three O atoms of the anion each make two N–H···O contacts shorter than 2.7 Å (2 × 2.26 Å; 2.00, 2.43 Å; 2.00, 2.43 Å) along the *a* and *b* directions. The remaining O atom makes two C–H···O contacts (2 × 2.65 Å) along the *c* direction, which become truncated at the *ab* plane surface. Thus, the arrangement of the higher-lying ClO_4^- anion, strongly bound to the chains by the N–H···O hydrogen bonds, is not likely to be affected by the loss of the weak C–H···O hydrogen bonds at the *ab* plane surface.

Figure 6b shows a projection view (along the *b* axis) of the N–H···O and C–H···O hydrogen bonds around the lower-lying ClO_4^- anion. Three O atoms of the anion each make short N–H···O contacts (2 × 2.15 Å; 2.43, 2.51, 2.66 Å; 2.43, 2.51, 2.66 Å). The remaining O atom makes two C–H···O contacts (2 × 2.52 Å) along the *a* direction and two C–H···O contacts (2 × 2.68 Å) along the *c* direction. The latter two hydrogen bonds are truncated at the *ab* plane surface. Thus, the N–H···O hydrogen bonds of the lower-lying ClO_4^- anion are longer than the corresponding ones for the higher-lying ClO_4^- anion, so that the lower-lying ClO_4^- anion is more weakly bound to the chains than is the higher-lying ClO_4^- anion.

Figure 6c shows a projection view (along the *b* axis) of the N–H···O and C–H···O hydrogen bonds around the lower-lying ClO_4^- anion when its position is rotated by the rearrangement step 1 defined in the previous section. Now, three O atoms of the anion each make very short N–H···O contacts (2 × 1.99 Å; 2.26, 2.66 Å; 2.27, 2.69 Å), and the remaining O atom makes short C–H···O contacts (2 × 2.27 Å) along the *c* direction. The latter two C–H···O hydrogen bonds are truncated at the *ab* plane surface, which allows the anion to slightly move out of the *ab* plane surface (i.e., the rearrangement step 2 defined in the previous section) and hence release the strain in the very short N–H···O contacts (2 × 1.99, 2.26, 2.27 Å) induced by the rearrangement step 1. Consequently, the rearrangement of the lower-lying ClO_4^- anion, invoked in the previous section to explain the anion patterns of the experimental AFM image, is an interesting example of surface reconstruction in which the anions optimize their N–H···O hydrogen bonding at the surface.

Concluding Remarks

The observed AFM images of both $[Pt(en)_2][Pt(en)_2I_2](ClO_4)_4$ and $[Pt(en)_2][Pt(en)_2(Br_{0.8}I_{0.2})_2](ClO_4)_4$ are dominated by bright spots representing the most protruded H atoms of the en ligands and the most protruded O atoms of the ClO_4^- anions. The AFM images of $[Pt(en)_2][Pt(en)_2I_2](ClO_4)_4$ possesses all the features of the *bc* plane surface expected from the bulk crystal structure, which means that there is no significant surface

(26) (a) Taylor, R.; Kennard, O. *J. Am. Chem. Soc.* **1982**, *104*, 5063. (b) Murray-Rust, P.; Glusker, J. P. *J. Am. Chem. Soc.* **1984**, *106*, 1018.

(27) (a) Sarma, J. A. R. P.; Desiraju, G. R. *Acc. Chem. Res.* **1986**, *19*, 222. (b) Desiraju, G. R. *Crystal Engineering: The Design of Organic Solids*; Elsevier: Amsterdam, 1989. (c) Desiraju, G. R. *Acc. Chem. Res.* **1991**, *24*, 290.

(28) Williams, J. M.; Ferraro, J. R.; Thorn, R. J.; Carson, K. D.; Geiser, U.; Wang, H. H.; Kini, A. M.; Whangbo, M.-H. *Organic Superconductors (Including Fullerenes)*; Prentice Hall: New York, 1992; Chapter 8.

(29) Pénicaud, A.; Boubekeur, K.; Batail, P.; Canadell, E.; Auban-Senzier, P.; Jérome, D. *J. Am. Chem. Soc.* **1993**, *115*, 4101.

reconstruction. However, this is not the case for $[Pt(en)_2][Pt(en)_2(Br_{0.8}I_{0.2})_2](ClO_4)_4$. Although the AFM image of the latter is essentially consistent with the *ab* plane surface expected from the bulk structure, the ClO_4^- anions are represented by spots of equal brightness instead of alternating bright and dim spots expected from the bulk crystal structure. This discrepancy suggests that, of the two kinds of the surface ClO_4^- anions, the lower-lying ones change their orientation and height. Analysis of the N–H···O and C–H···O contacts associated with the ClO_4^- anions shows that this rearrangement optimizes their N–H···O hydrogen bonding.

Acknowledgment. Work at Los Alamos National Laboratory and North Carolina State University were both supported by the Office of Basic Energy Sciences, Division of Materials Science, U.S. Department of Energy.

CM940441F